Coulomb scattering rates of excited states in monolayer electron-doped germanene

Po-Hsin Shih,[1] Chih-Wei Chiu,[2] Jhao-Ying Wu,[3,*] Thi-Nga Do,[2] and Ming-Fa Lin[4,5,†]
[1]*Department of Physics, National Cheng Kung University, Tainan 701, Taiwan*
[2]*Department of Physics, National Kaohsiung Normal University, Kaohsiung 824, Taiwan*
[3]*Center of General Studies, National Kaohsiung Marine University, Kaohsiung 811, Taiwan*
[4]*Hierarchical Green-Energy Materials Research Center, National Cheng Kung University, Tainan 701, Taiwan*
[5]*Quantum Topology Center, National Cheng Kung University, Tainan 701, Taiwan*

(Received 16 October 2017; revised manuscript received 6 January 2018; published 3 May 2018)

Excited conduction electrons, conduction holes, and valence holes in monolayer electron-doped germanene exhibit unusual Coulomb decay rates. The deexcitation processes are studied using the screened exchange energy. They might utilize the intraband single-particle excitations (SPEs), the interband SPEs, and the plasmon modes, depending on the quasiparticle states and the Fermi energies. The low-lying valence holes can decay through the undamped acoustic plasmon, so that they present very fast Coulomb deexcitations, nonmonotonous energy dependence, and anisotropic behavior. However, the low-energy conduction electrons and holes are similar to those in a two-dimensional electron gas. The higher-energy conduction states and the deeper-energy valence ones behave similarly in the available deexcitation channels and have a similar dependence of decay rate on the wave vector **k**.

DOI: 10.1103/PhysRevB.97.195302

I. INTRODUCTION

A lot of two-dimensional (2D) materials have been successfully synthesized since the first discovery of graphene in 2004 using the mechanical exfoliation of Bernal graphite [1]. They are very suitable for exploring diverse physical, chemical, and material properties. Specifically, the 2D group-IV systems possess a high-symmetry honeycomb lattice and nanoscale thickness, in which few-layer graphenes have been verified to exhibit rich and unique properties, such as massless and massive fermions [2–5], quantized Landau levels [6–9], magneto-optical selection rules [10–13], and quantum Hall effects [14–17]. Recently, few-layer germanene, silicene, and tinene were, respectively, grown on [Pt(111), Au(111), and Al(111)] surfaces [18–21], [Ag(111), Ir(111), and $\mathrm{ZrBi_2}$] surfaces [22–24], and the $\mathrm{Bi_2Te_3}$(111) surface [25]. Monolayer germanene and silicene, with a stable $\sqrt{3} \times \sqrt{3}$ geometric structure, have been clearly identified from scanning tunnel microscopy measurements [20,21]. Such systems possess buckled structures and significant spin-orbital couplings (SOCs), leading to rich and unique essential properties [26,27]. They are expected to present unusual Coulomb excitations and deexcitations arising from many-particle electron-electron interactions. The Coulomb scattering rates of the excited states in monolayer electron-doped germanene are chosen for a model study in this work, especially for their relations with single-particle and collective electronic excitations.

For germanene, silicene, and graphene, the low-lying electronic structures mainly arise from the outermost p_z orbitals [4,27]. The Dirac-cone structures, being created by the hexagonal symmetry, might be separated or gapless as a result of significant or negligible SOCs. From an effective Hamiltonian of the tight-binding model [discussed later in Eq. (1)] [27–30], germanene and silicene are predicted to be narrow-gap semiconductors with band gaps of $E_g \sim 93$ and $\sim$7.9 meV, respectively, reflecting the strengths of SOCs. Moreover, the first-principles calculations indicate that the extra Ge adatoms on monolayer germanene could form dumbbell reconstruction structures [31], and there exist very complicated energy bands initiating from the distinct high-symmetry points. On the other hand, graphene has linear valence and conduction bands intersecting at the Dirac point in the absence of SOC. The calculated band structures could be examined from the angle-resolved photoemission spectroscopy (ARPES) measurements, as done for few-layer germanene grown on a Au(111) surface [19]. Experimental observations indicate that the multiple Dirac-like energy dispersions might be caused by the folding of germanene's Dirac cones. High-resolution ARPES measurements also provide complete information on the energy widths of the excited states [19,32,33].

Electron-electron interactions are one of the mainstream topics in condensed-matter systems [34–38] since they are responsible for a lot of physical properties, e.g., the effective Coulomb potential, the impurity screening, the correlation energy, the effective mass, and the mean free path. The Coulomb interactions create the many-particle electronic excitations and thus have strong effects on the energies and lifetimes of quasiparticle states. Previous calculations predicted that monolayer electron-doped germanene exhibits diverse momentum- and frequency-dependent phase diagrams [38]. Rich Coulomb excitations, as shown Figs. 1(a) and 1(b) at $E_F = 0.2$ eV, cover the anisotropic excitation spectra, the intraband single-particle excitations (SPEs), the interband SPEs, the strong acoustic plasmon at small momenta q's, the second kind of plasmon

---

[*] Corresponding author: yarst5@gmail.com

[†] Corresponding author: mflin@mail.ncku.edu.tw

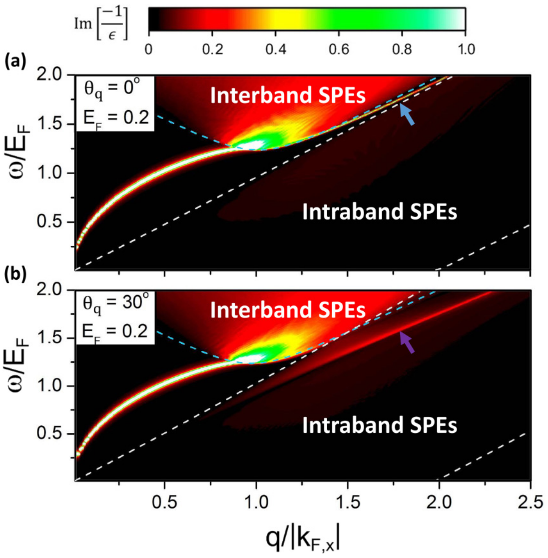

FIG. 1. The momentum- and frequency-dependent excitation spectra of germanene with $E_F = 0.2$ eV under (a) $\theta_q = 0^\circ$ and (b) 30°, in which θ_q is the angle between the transferred momentum and ΓM [Fig. 2(b)]. The second and third kinds of plasmon modes are, respectively, indicated by the blue and purple arrows in (a) and (b). $k_{F,x}$ is the Fermi momentum along ΓM.

[the undamped mode at large q's by the blue arrow in Fig. 1(a)], and the third kind of plasmon accompanied by the intraband Landau damping [the purple arrow in Fig. 1(b)]. They might become the effective deexcitation channels of the excited electrons (holes), depending on the wave vectors, valence (conduction) states, and Fermi energies. The main features and mechanisms of the Coulomb decay rates and the significant differences among the emergent 2D materials is worthy of a systematic investigation.

The screened exchange energy characterized by Matsubara's Green's functions is used to calculate the Coulomb scattering rates of the excited states in monolayer electron-doped germanene, in which the deexcitation channels are evaluated from the random-phase approximation (RPA). The decay processes and their dependence on the wave vector, valence and conduction states, and Fermi energy (doping density) are explored in detail. A comparison with monolayer graphene is also made. This work shows that the intraband SPEs, the interband SPEs, and the distinct plasmon modes play critical roles in determining the deexcitation behaviors. The unusual Coulomb decay rates are revealed as the oscillatory energy dependence, the strong anisotropy, the nonequivalent valence and conduction Dirac points, and the similarity to a 2D electron gas for the low-energy conduction electrons and holes. The predicted Coulomb decay rates could be directly verified from the high-resolution ARPES measurements on the energy widths of the quasiparticle state at low temperatures [19,32,33].

This work is organized as followings. The zero-field Hamiltonian and the RPA self-energy of monolayer electron-doped germanene are derived and discussed in Sec. II. Section III covers the evaluated Coulomb decay rates, the fundamental mechanisms, the experimental examinations, and the comparisons with graphene. Section IV gives concluding remarks, accompanied by the effects due to the electron-hole asymmetry, the measured $\sqrt{3} \times \sqrt{3}$ structure, and the predicted dumbbell reconstruction structures.

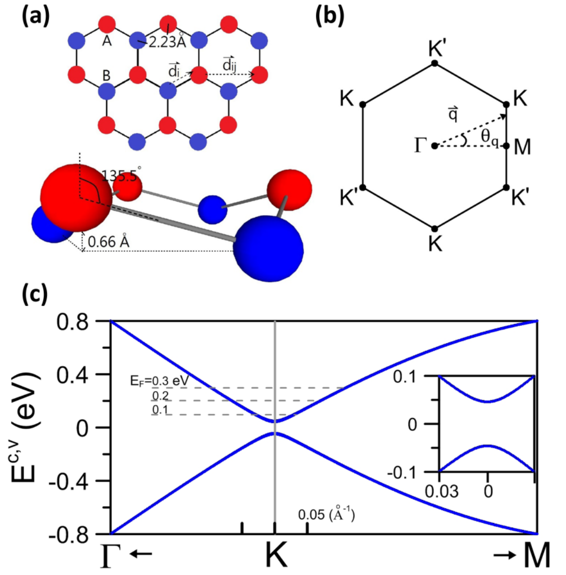

FIG. 2. (a) Geometric structure of monolayer germanene shown in the top and side views, (b) the first Brillouin zone, and (c) low-lying energy bands along the high-symmetry points, accompanied by those near the Dirac points in the inset.

II. THE RPA SELF-ENERGY

Monolayer germanene has a buckled hexagonal lattice with a Ge-Ge bond length of $b = 2.32$ Å, as shown in Fig. 2(a). There are two equivalent sublattices, A and B, separated by a distance of $l = 0.66$ Å (details are given in [38]). The low-lying electronic structure is dominated by $4p_z$ orbitals. The Hamiltonian, which is built from the subspace spanned by the four spin-dependent tight-binding functions, is expressed as

$$H = -t \sum_{\langle i,j\rangle,\alpha} c^\dagger_{i\alpha} c_{j\alpha} + i\frac{\lambda_{so}}{3\sqrt{3}} \sum_{\langle\langle i,j\rangle\rangle,\alpha,\beta} \nu_{ij} c^\dagger_{i\alpha} \sigma^z_{\alpha\beta} c_{j\beta} - i\frac{2}{3}\lambda_R \sum_{\langle\langle i,j\rangle\rangle,\alpha,\beta} \mu_{ij} c^\dagger_{i\alpha} (\vec{\sigma} \times \hat{d}_{ij}) c_{j\beta}. \tag{1}$$

The first term, the summation over all the pairs $\langle i,j\rangle$ of the nearest-neighbor lattice sites, is the kinetic energy with a hopping integral of $t = 0.86$ eV [27]; $c^\dagger_{i\alpha}$ ($c_{j\alpha}$) can create (annihilate) an electron with spin polarization α (β) at the ith (jth) site. The second term represents the effective SOC with the summation over all pairs $\langle\langle i,j\rangle\rangle$ of the next-nearest-neighbor sites, and its strength is $\lambda_{SO} = 46.3$ meV. $\vec{\sigma} = (\sigma_x, \sigma_y, \sigma_z)$ is the Pauli spin matrix. $\nu_{i,j} = (\vec{d}_i \times \vec{d}_j)/|\vec{d}_i \times \vec{d}_j|$, where $\nu_{i,j} = +1$ and -1, respectively, correspond to the counterclockwise and clockwise cases from the cross product of the two nearest-neighbor bonding vectors $\vec{d}_i$ and $\vec{d}_j$. The third term denotes the Rashba SOC with $\lambda_R = 10.7$ meV, $u_{i,j} = +1$ (-1) for the A (B) lattice sites, and $\hat{d}_{ij}$ is the unit vector connecting two sites, i and j, in the same sublattice [Fig. 2(a)]. State energies are characterized by $E^{c,v}(\mathbf{k})$ [$E^h(\mathbf{k})$], where c and v represent conduction and valence states, respectively. They remain doubly degenerate for the spin degree of freedom in the presence of SOC, in which there exists spin-up- and spin-down-dominated configurations.

The free-carrier density and temperature can greatly enrich the electronic excitations of monolayer germanene. Under the perturbation of Coulomb interactions, electrons are excited from the occupied states to the unoccupied ones during the dynamic charge screening. For an intrinsic germanene, only the interband SPEs, described by the imaginary part of the dielectric function, can survive at zero temperature. The collective excitations are revealed in the loss function as a prominent peak when the free-carrier density or temperature is sufficiently high [38]. The extrinsic germanene, with electron doping, is predicted to exhibit three kinds of plasmon modes. There exist intraband and interband SPEs [Figs. 1(a) and 1(b)], in which the former and the latter are, respectively, associated with the conduction and valence carriers. The first kind of plasmon, which behaves as a 2D acoustic mode at small transferred momenta, will make a large contribution to Coulomb decay rates. At large q's, it experiences heavy interband Landau damping and then disappears. Specifically, the second and third kinds of plasmons come to exist only under sufficiently large momenta. The above-mentioned single- and many-particle excitation channels are available in the inelastic Coulomb scatterings, as discussed later.

The incident electron beam or electromagnetic field has strong interactions with charge carriers and thus creates the excited electrons (holes) above (below) the Fermi level. Such intermediate states could further decay via the inelastic electron-electron scatterings. The Coulomb decay rate $1/\tau$ is dominated by the effective interaction potential V^{eff} between two charges, in which the dynamic e-e interactions can be understood from the RPA. By using the Matsubara Green's functions [39], $1/\tau$ is evaluated from the quasiparticle self-energy, the screened exchange energy

$$\Sigma(\mathbf{k},h,ik_n) = -\frac{1}{\beta}\sum_{\mathbf{q},h',i\omega_m} V^{\mathrm{eff}}(\mathbf{q},i\omega_m;\mathbf{k},h,h')G^{(0)} \times(\mathbf{k}+\mathbf{q},h',ik_n+i\omega_m), \tag{2}$$

where $\beta=(k_BT)^{-1}$, $ik_n=i(2n+1)\pi/\beta$ (complex fermion frequency), $i\omega_m=i2m\pi/\beta$ (complex boson frequency), and $G^{(0)}$ is the noninteracting Matsubara Green's function. $V^{\mathrm{eff}}(\mathbf{q},i\omega_m;h,h',\mathbf{k})=V_q|\langle h',\mathbf{k}+\mathbf{q}|e^{i\vec{q}\cdot\vec{r}}|h,\mathbf{k}\rangle|^2/[\epsilon(\mathbf{q},\mathrm{i}\omega_m)]=V(\mathbf{q};h,h',\mathbf{k})/[\epsilon(\mathbf{q},i\omega_m)]$ is the screened Coulomb interaction with the band-structure effect, where V_q is the 2D bare Coulomb potential energy and $\epsilon(\mathbf{q},i\omega_m)$ is the RPA dielectric function. It should be noted that the SOC leads to the superposition of the spin-up and spin-down components. However, it does not need to deal with the spin-up- and spin-down-dependent Coulomb decay rates separately since they make the same contribution. That is, it is sufficient to explore the wave-vector-, conduction- and valence-, and energy-dependent self-energy [Eq. (2)]. Under the analytic continuation $ik_n\rightarrow E^h(\mathbf{k})$, the self-energy can be divided into the line part and the residue part:

$$\Sigma(\mathbf{k},h,E^h(\mathbf{k})) = \Sigma_x(\mathbf{k},h)+\Sigma^{(\mathrm{line})}(\mathbf{k},h,E^h(\mathbf{k})) + \Sigma^{(\mathrm{res})}(\mathbf{k},h,E^h(\mathbf{k})) \tag{3}$$

in which

$$\Sigma_x(\mathbf{k},h) = -\sum_{\mathbf{q},h'} V(\mathbf{q};h,h',\mathbf{k})n_F(E^{h'}(\mathbf{k}+\mathbf{q})) \tag{4}$$

$$\begin{aligned}\Sigma^{(\mathrm{line})}&(\mathbf{k},h,E^h(\mathbf{k}))\\ &= -\frac{1}{\beta}\sum_{\mathbf{q},h',i\omega_m}[V^{\mathrm{eff}}(\mathbf{q},i\omega_m;\mathbf{k},h,h')-V(\mathbf{q};h,h',\mathbf{k})]\\ &\quad\times G^{(0)}(\mathbf{k}+\mathbf{q},h',E^h(\mathbf{k})+i\omega_m)\end{aligned} \tag{5}$$

and

$$\begin{aligned}\Sigma^{(\mathrm{res})}&(\mathbf{k},h,E^h(\mathbf{k}))\\ &= -\frac{1}{\beta}\sum_{\mathbf{q},h',i\omega_m}[V^{\mathrm{eff}}(\mathbf{q},i\omega_m;\mathbf{k},h,h')-V(\mathbf{q};h,h',\mathbf{k})]\\ &\quad\times[G^{(0)}(\mathbf{k}+\mathbf{q},h',\mathrm{i}k_n+i\omega_m)\\ &\quad-G^{(0)}(\mathbf{k}+\mathbf{q},h',E^h(\mathbf{k})+i\omega_m)].\end{aligned} \tag{6}$$

The imaginary part of the residue self-energy determines the Coulomb decay rate and is defined as

$$\begin{aligned}\mathrm{Im}\Sigma^{(\mathrm{res})}(\mathbf{k},h,E^h(\mathbf{k})) &= \frac{-1}{2\tau(\mathbf{k},h)}\\ &= \sum_{\mathbf{q},h'}\mathrm{Im}[-V^{\mathrm{eff}}(\mathbf{q},\omega_{de};\mathbf{k},h,h')]\\ &\quad\times\{n_B(-\omega_{de})[1-n_F(E^{h'}(\mathbf{k}+\mathbf{q}))]\\ &\quad-n_B(\omega_{de})[n_F(E^{h'}(\mathbf{k}+\mathbf{q}))]\}\\ &= \frac{-1}{2\tau_e(\mathbf{k},h)}+\frac{-1}{2\tau_h(\mathbf{k},h)}.\end{aligned} \tag{7}$$

$\omega_{de}=E^h(\mathbf{k})-E^{h'}(\mathbf{k}+\mathbf{q})$ is the deexcitation energy. n_B and n_F are the Bose-Einstein and Fermi-Dirac distribution functions, respectively. Equation (7) indicates that an initial state of $(\mathbf{k},h)$ can be deexcited to all the available $(\mathbf{k}+\mathbf{q},h')$ states under the Pauli exclusion principle and the conservation of energy and momentum. The excited states above and below the Fermi level are, respectively, related to the electron and hole decay rates [the first and second terms in Eq. (7)]. From detailed calculations, the zero-temperature Coulomb decay rates of the excited electrons and holes are

$$\begin{aligned}\frac{1}{\tau_e(\mathbf{k},h)}+\frac{1}{\tau_h(\mathbf{k},h)} &= -2\sum_{\mathbf{q},h'}\mathrm{Im}[-V^{\mathrm{eff}}(\mathbf{q},\omega_{de};\mathbf{k},h,h')]\\ &\quad\times\{-\Theta(\omega_{de})\Theta[E^{h'}(\mathbf{k}+\mathbf{q})-E_F].\\ &\quad+\Theta(-\omega_{de})\Theta[E_F-E^{h'}(\mathbf{k}+\mathbf{q})]\},\end{aligned} \tag{8}$$

where E_F is the Fermi energy. Θ is the step function that describes the available deexcitation channels. In addition, the decay rate is double the energy width of the quasiparticle state.

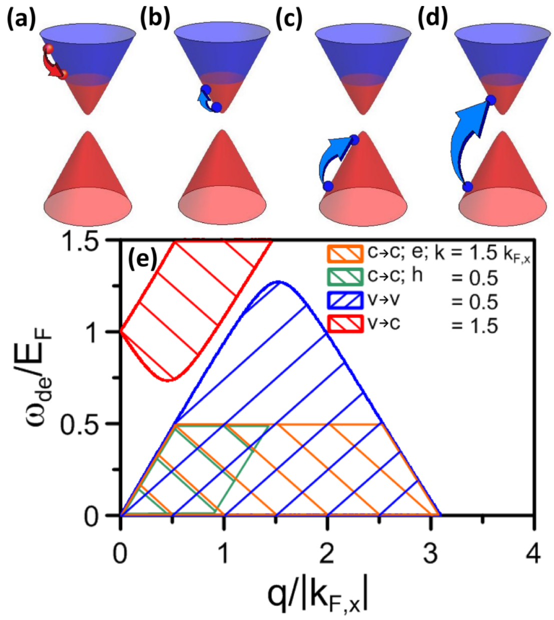

FIG. 3. The available deexcitation channels of the specific excited states are indicated for (a) the conduction electrons, (b) the conduction holes, and the valence holes scattered into the (c) same and (d) distinct bands. (e) The relations between the deexcitation energies and transferred momenta.

III. COULOMB DECAY RATES

Germanene displays a feature-rich band structure due to significant SOC and the buckled honeycomb lattice. The conduction band is symmetric to the valence one about zero energy under an effective Hamiltonian in Eq. (1) [Fig. 2(c)]. These two bands present parabolic energy dispersions near the K point [Fig. 2(b)], in which the separated Dirac points have an energy spacing of $E_D = 93$ meV because of SOC [inset in Fig. 2(c)]. The state energy $E^h(\mathbf{k})$ is measured from the middle of the energy spacing. Energy bands are gradually changed into linear dispersions with the increase of state energy. The band structure is anisotropic at sufficiently high energies ($|E^{c,v}| > 0.2$ eV), as observed along the $K\Gamma$ and KM directions. With the increasing wave vector, the former exhibits more obvious changes compared with the latter. The anisotropic energy spectrum will play an important role in the Coulomb scatterings related to the available deexcitation channels.

The Fermi energy dominates the main features of electronic excitations and thus determines the Coulomb decay channels. When E_F is in the middle of energy spacing, the excited electrons or holes at zero temperature can decay into conduction or valence band states only by using the interband SPEs. The increase in E_F creates the intraband SPEs and plasmon modes and induces the drastic changes in the interband SPEs. Such Coulomb excitations can greatly diversify the decay channels. As for the excited conduction electrons, the final states during the Coulomb deexcitations lie between only the initial states and the Fermi momentum [red arrow in Fig. 3(a)], according to the Pauli exclusion principle and the conservation of energy and momentum. The available deexcitation channels, the intraband SPEs, make the most important contributions to the Coulomb decay rates for the low-lying conduction electrons, corresponding to the orange part in Fig. 3(e). But when the initial-state energy is high, the interband SPEs and the second or third kind of plasmon modes might become the effective deexcitation mechanisms [discussed later in Figs. 4(c) and 5(a)]. Concerning the excited holes in the conduction band, they can be deexcited to the conduction states [$c \rightarrow c$; blue arrow in Fig. 3(b)] through the intraband SPEs, mainly owing to the low deexcitation energies and transferred momenta, as shown by the green part in Fig. 3(e). On the other hand, the valence holes present two kinds of decay processes: $v \rightarrow v$ and $v \rightarrow c$ in Figs. 3(c) and 3(d), respectively. Their available decay channels cover intraband SPEs, interband SPEs, and the second or third kind of plasmon modes and the interband SPEs and acoustic plasmon modes, respectively, corresponding to the blue and red parts in Fig. 3(e). Specifically, the latter has large deexcitation energies at small momenta and is thus expected to exhibit efficient and unusual Coulomb decay rates.

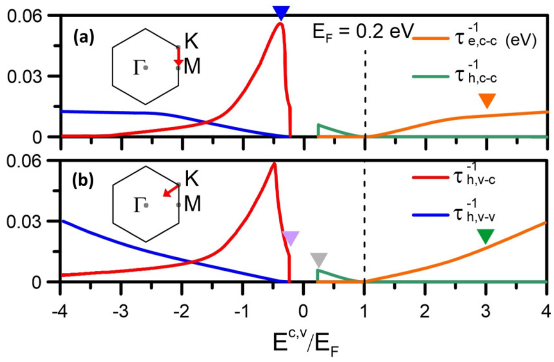

FIG. 4. The Coulomb decay rates of the quasiparticle states along the special directions of (a) KM and (b) $K\Gamma$ are taken into consideration under $E_F = 0.2$ eV.

The Coulomb decay rates are very sensitive to the quasiparticle state ($\mathbf{k}$, h). As to the excited conduction electrons, the $c \rightarrow c$ intraband process is available as state energy gradually increases from the Fermi level. The intraband SPEs make the

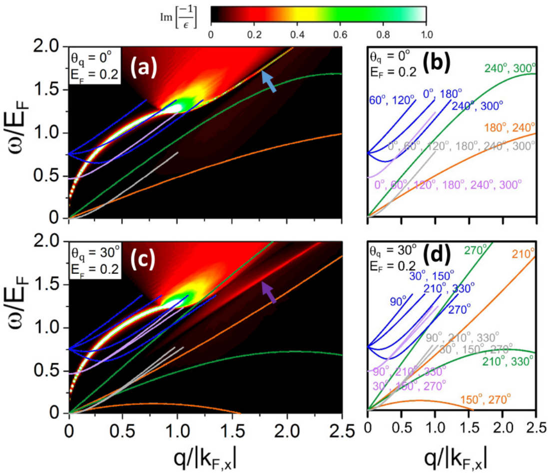

FIG. 5. The available deexcitation spectra due to the specific states indicated by the arrows in Figs. 4(a) and 4(b) are shown for (a) $\theta_q = 0^\circ$ and (c) $\theta_q = 30^\circ$. (b) and (d) The details of the θ_q-dependent deexcitation energies. The curves are defined by the conservation of energy and momentum.

main contributions to this process [the orange part in Fig. 3(e)]; therefore, the decay rate monotonously grows with E^c, as shown in Figs. 4(a) and 4(b) by the orange curves. When the excited states are close to E_F ($|E^c - E_F| \leqslant 0.5E_F$), $1/\tau_e$ is roughly proportional to $(E^c - E_F)^2 \ln|E^c - E_F|$, according to the numerical fitting. Such an energy dependence is characteristic of a 2D electron gas [40,41]. This is not surprising since as $E^c \rightarrow E_F$, the deexcitation energy is essentially linear in q whether the energy band has a linear or a quadratic energy dispersion. Furthermore, the low-momentum-frequency intraband SPEs are the only deexcitation channels. It is for such reasons that the widths of germanene and an electron gas near the Fermi level share a similar character.

For the higher-energy conduction states, the Coulomb decay rates depend on the anisotropic energy bands. Along the KM direction [Fig. 4(a)], $1/\tau_e$ increases and then reaches a saturated value after $E^c > 3E_F$ (orange arrow). But for the $K\Gamma$ direction [Fig. 4(b)], it gets large with the further increase of E^c (green arrow). This important difference between the two directions lies in whether the interband SPEs are the effective deexcitation channels. The higher-energy electronic states have stronger energy dispersions along $K\Gamma$ [Fig. 2(c)], so that their deexcitation energies at large transferred momenta are consistent with those of the interband SPEs. For example, the conduction state of $E^c = 3E_F$ along $K\Gamma$ has a lot of deexcitation channels, indicated by the green curve in Fig. 5(a) at $\theta_q = 0^\circ$. Similar results are revealed in different momentum directions, e.g., the green curves at $\theta_q = 30^\circ$ in Fig. 5(c). The effective deexcitation channels cover the intraband and interband SPEs. The latter is responsible for the enhanced Coulomb decay rates in the high-energy conduction states along $K\Gamma$. On the other hand, the $E^c = 3E_F$ conduction electron along KM has lower deexcitation energies and thus exhibits only intraband SPEs, as illustrated by the orange curves in Figs. 5(a) and 5(c).

The deexcitation behaviors of the excited holes strongly depend on whether they belong to conduction or valence states. Concerning the conduction holes, the Coulomb decay rates are isotropic, as indicated by the almost identical $\tau^{-1}_{h,c-c}$'s along KM and $K\Gamma$ [green curves in Figs. 4(a) and 4(b)]. Furthermore, the energy dependence is similar to that of the low-lying conduction electrons (2D electron gas). Such results directly reflect the fact that the intraband SPEs are the only available deexcitation channels, e.g., the gray curves related to the conduction Dirac point [Figs. 5(a) and 5(c)]. Specifically, the K point [gray arrow in Fig. 4(b)] has the largest Coulomb decay rate among all the excited conduction holes.

On the other hand, the decay rates of the valence holes exhibit unusual **k** dependences. The valence Dirac point has a significant decay rate [purple arrow in Fig. 4(b)], being much higher than that of the conduction one. It presents only the $v \rightarrow c$ decay process, in which the deexcitation channels mainly come from the interband SPEs and the undamped plasmon modes, as indicated by the purple curves in Figs. 5(a) and 5(c). They create the important difference between the valence and conduction Dirac points. With the increase of the valence-state energy, two decay processes, $v \rightarrow c$ and $v \rightarrow v$, contribute to the Coulomb decay rates simultaneously. As to the former, the available range of the strong acoustic plasmon grows and then decreases quickly for the low-lying valence holes, leading to an unusual peak structure in $\tau^{-1}_{h,v-c}$ at small E^v's [the red curve in Figs. 4(a) and 4(b)]. For example, the $E^v = -0.4E_F$ valence state along KM has the widest plasmon-decay range, associated with the blue curves in Figs. 5(a) and 5(c), so it can exhibit fast Coulomb decay [blue arrow in Fig. 4(a)]. The plasmon-induced deexcitations are almost absent for the deeper valence states (e.g., $E^v < -1.5E_F$ along KM). The interband SPEs also make some contributions to $\tau^{-1}_{h,v-c}$, and they dominate the Coulomb decay rates of the deeper-energy states, e.g., the red curves along KM and $K\Gamma$ at $E^v < -2E_F$. Specifically, for the $v \rightarrow v$ process, the excited valence holes [the blue curves in Figs. 4(a) and 4(b)] behave as the excited conduction electrons (the orange curves) in terms of the **k** dependence and the deexcitation channels. The intraband SPEs are the dominating mechanisms in determining $\tau^{-1}_{h,v-v}$ of the low-lying valence states ($E^v > -2E_F$). They are replaced by the intraband SPEs and interband SPEs for the deeper valence states along $K\Gamma$. This accounts for the anisotropic Coulomb decay rates along $K\Gamma$ and KM.

The effective deexcitation channels deserve closer examination. Each excited state could decay along any direction, as clearly indicated by the summation of $\mathbf{q}$ in Eq. (7), in which the transferred momentum is a function of q (magnitude) and θ_q (azimuthal angle in the range of 2π). By means of the specific excitation spectrum, it might exhibit several dispersion relations (less than six) in the q-dependent deexcitation energies for a fixed θ_q. The main reason is that the Coulomb excitations and energy bands possess hexagonal symmetry; that is, the excitation spectra are identical for θ_q, $\theta_q + \pi/3$, $\theta_q + 2\pi/3$, $\theta_q + 3\pi/3$, $\theta_q + 4\pi/3$, and $\theta_q + 5\pi/3$. For example, the excited valence hole state, with the highest Coulomb decay rate along KM ($K\Gamma$), shows three (four) independent dispersive functions (blue curves) for $\theta_q = 0^\circ$ ($\theta_q = 30^\circ$). The other excited states in Figs. 5(a) and 5(c) exhibit similar behaviors. The total deexcitation regions consist of θ_q-dependent dispersion relations; that is, they are very sensitive to the direction and magnitude of $\mathbf{q}$, as expected from the basic scattering pictures. Specifically, Figs. 5(a) and 5(c) clearly show that the excited states along KM and $K\Gamma$ do not utilize the second and third plasmons as the effective deexcitation channels since the deexcitation energies are insufficient. However, the excited electrons along $K\Gamma$, with energies higher than $5E_F$, could decay via the second kind of plasmon mode (not shown). If they are in between KM and $K\Gamma$, their energies larger than $3E_F$ will be able to deexcite via the third kind of plasmon mode.

The wave-vector- and Fermi-energy-dependent Coulomb scattering rates, as clearly shown in Figs. 6(a)–6(f), deserve closer examination. The decay rates of the valence holes exhibit oscillatory energy dependence along any wave-vector directions, mainly owing to the complicated deexcitation channels. The strongest Coulomb scatterings, being associated with the undamped acoustic plasmons, appear at valence states below the Dirac point [the dashed blue curves in Figs. 6(a), 6(c), and 6(e)]. The valence-state decay rates strongly depend on the direction of **k**, in which they are, respectively, lowest and highest along KM and $K\Gamma$. Apparently, anisotropic Coulomb decay rates exist for any valence-state energies. This is closely related to the strong anisotropy of the deeper valence band [Fig. 2(c)]. As for conduction holes and electrons, the

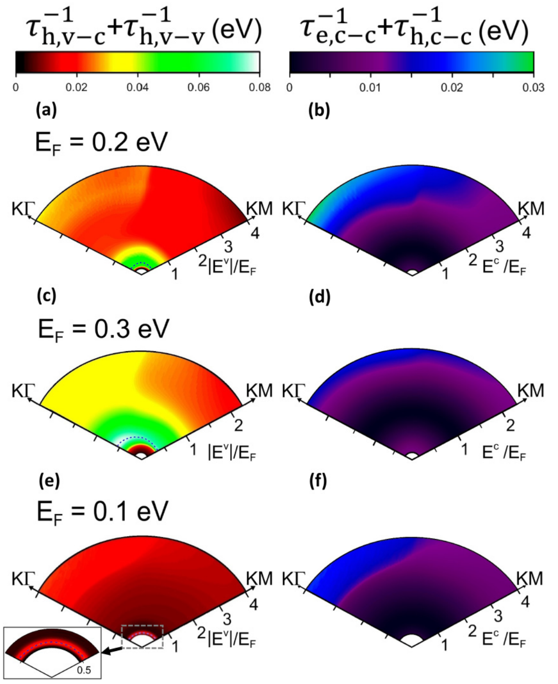

FIG. 6. The wave-vector-dependent Coulomb scattering rates of (a) the valence holes and (b) the conduction holes and electrons at $E_F = 0.2$ eV. Similar plots at (c) and (d) $E_F = 0.3$ eV and (e) and (f) 0.1 eV.

Coulomb scattering rates, as measured from that of the Fermi-momentum state, present monotonous energy dependences. The anisotropic deexcitations come to exist only for the higher-energy conduction states.

It is relevant to observe the oscillatory energy dependence and the anisotropic behavior at higher Fermi energy. Electronic excitations and Coulomb decay rates are very sensitive to the changes in free-carrier densities, as revealed in Fig. 6. The momentum-frequency excitation spectra are drastically altered by the Fermi energy. For example, a fully undamped intraband plasmon, almost isotropic excitations, and an obvious excitation gap between the intra- and interband SPEs are revealed at a sufficiently low Fermi level, e.g., excitation spectra at $E_F = 0.1$ eV [38]. These are directly reflected in the Coulomb decay rates. For larger E_F, the available momentum-frequency deexcitation range of the strongest acoustic plasmons and the interband SPEs is enhanced since they could coexist. This leads to a stronger dependence of decay rates on the state energy and direction of $\mathbf{k}$, as clearly indicated in Fig. 6(c) at $E_F = 0.3$ eV and Fig. 6(e) at $E_F = 0.1$ eV. The E_F-induced differences are further illustrated by the Coulomb decay rates of the specific states. For example, the largest decay rates are, respectively, 0.074 and 0.081 eV along KM and $K\Gamma$ at $E_F = 0.3$ eV, while they become 0.022 and 0.024 eV at $E_F = 0.1$ eV. Furthermore, the conduction and valence Dirac points present similar differences in the magnitude of decay rate and anisotropic behavior.

The effective Hamiltonian in Eq. (1) and the RPA self-energy in Eqs. (2)–(8) are suitable for monolayer germanene, silicene, and graphene, with p_z-dominated band structures. The first system possesses the smallest hopping integral and the largest SOC, so that the essential properties are relatively easily tuned by the external factors, e.g., the carrier doping, electric field, and magnetic field. Specifically, graphene, with the strongest hopping integral (~2.6 eV), exhibits a pair of linearly intersecting valence and conduction bands at the gapless Dirac points in the absence of SOC, in which the isotropic Dirac-cone structure is further used to investigate the rich and unique physical properties [42–45]. However, there are important differences between germanene and graphene in electronic excitations and Coulomb decay rates. Germanene is predicted to present the anisotropic excitation spectra, the second and third kinds of plasmons, a fully undamped acoustic plasmon under low doping, and the SOC-dependent excitation boundaries. Such features are absent in graphene [38]. The theoretical calculations have been done for the excited conduction and valence electrons in graphene, indicating the isotropic behavior and vanishing Coulomb decay rate at the Dirac point [45]. Apparently, the calculated results are different from those in this work.

The predicted scattering decay rates can be examined from the high-resolution ARPES measurements, as successfully done for potassium adsorption on monolayer graphene [33]. The ARPES spectra are measured along the KM and $K\Gamma$ directions for various doping concentrations in monolayer electron-doped graphene, clearly indicating the quasiparticle energy dispersions and the linewidth variations. They are further utilized to get the doping-dependent momentum distribution curves (MDCs). The Lorentzian peak structures are centered at the quasiparticle energies, and they present the full width at half maximum identified as $-2\text{Im}\,\Sigma^{(\text{res})}$ (the scattering rate). The SPEs and plasmons, as well as the electron-phonon scatterings at finite temperatures, are proposed to explain the unusual energy dependences of MDC linewidths. The ARPES measurements at low temperatures could provide the Coulomb-scattering-dominated MDCs to verify the theoretical predictions. The experimental examinations on monolayer electron-doped germanene are useful in understanding the main features of Coulomb decay rates and the critical deexcitation mechanisms.

IV. CONCLUDING REMARKS

In this work, the Coulomb scattering rates in monolayer electron-doped germanene were investigated using the screened exchange energy, in which the excitation spectra are evaluated within the RPA. The excited states cover the conduction electrons, conduction holes, and valence holes, creating the decay processes $c \to c$, $c \to c$, and $v \to c$ plus $v \to v$, respectively. The low-lying conduction electrons and holes present isotropic scattering rates, mainly owing to the dominating intraband SPEs. Furthermore, they behave as a 2D electron gas in the energy-dependent Coulomb decay rates. The other excited states exhibit rich and unique $\mathbf{k}$ dependence, including the oscillatory energy dependence and strong anisotropy. Specifically, the low-energy valence states have the largest decay rates by means of the undamped acoustic plasmon modes, especially for that along $K\Gamma$. Such deexcitation modes also lead to the important difference between the valence and conduction Dirac points. The deeper valence states and the higher conduction states have similar deexcitation channels, and so do the **k**-dependent decay rates. The intraband SPEs are replaced by the intraband SPEs, the interband SPEs, and the second and third kinds of plasmon modes during the variation from the KM to $K\Gamma$ direction. This is responsible for the anisotropic decay rates. It is relatively easy to observe the unusual Coulomb decay rates at higher Fermi energies. Germanene is different from graphene in excitation spectra and decay rates, being closely related to the strengths of the hopping integral and SOC. The theoretical predictions about energy-band-dominated Coulomb decay rates can be examined from the APRES measurements on the energy widths of quasiparticle states.

As to the symmetric electron-hole band structure [Fig. 2(c)], the momentum- and frequency-dependent excitation spectra are identical for electron and hole dopings, and so are the Coulomb scatterings. That is, the Coulomb decay rates of the excited conduction electrons, conduction holes, and valence holes are the same as those of the excited valence holes, valence electrons, and conduction electrons under the interchange of electron and hole dopings, respectively. On the other hand, the asymmetric valence and conduction bands about the zero energy might be induced by the partial multiorbital hybridization (the weak sp^3 bonding), the complicated interlayer hopping integrals in a buckled system, and the significant interactions with the substrate [46,47]. They might have significant effects on electronic excitations, including the momentum-frequency ranges of intraband and interband SPEs, the diversified plasmon modes (with splitting), the existence of Landau damping (the coexistence of plasmons and SPEs), the spectral anisotropy due to the momentum direction, and the distinct excitation spectra for electron and hole dopings [48]. The available deexcitation channels will become more complicated; therefore, the main features of Coulomb decay rates, the oscillatory energy dependence, and the anisotropic behavior, are expected to be greatly enhanced.

The geometric structures strongly affect the energy bands and thus the electron-electron Coulomb interactions. The measured $\sqrt{3} \times \sqrt{3}$ geometric structure [20,21] will induce the zone-folding effect on the band structure. More energy subbands and even energy spacings could create complicated excitation spectra and Coulomb scatterings, such as the various intraband and interband single-particle excitations and deexcitations, and the subband-dominated Coulomb decay rates. Concerning the predicted dumbbell structures [31], the distinct energy bands near the K, Γ, and M points arise from the multiorbital bondings due to the highly buckled structure. Their band structures are quite different from that of the pristine system, and so are the other essential properties. The Coulomb excitations and deexcitations will be dramatically changed in terms of the momentum-frequency excitation phase diagrams and the symmetry-point-dependent decay rates.

The RPA is frequently used to study the Coulomb excitations and deexcitations of condensed-matter systems, especially for high-density carriers in three-, two-, and one-dimensional materials [34–38,43–45]. This method might induce poor results at low free-carrier density in certain many-particle properties, mainly owing to insufficient correlation effects. Some models have been proposed to modify the electron-electron interactions, e.g., the Hubbard and Singwi-Sjolander models for electronic excitation spectra and the Ting-Lee-Quinn model for Coulomb decay rates [39]. The time-dependent first-principles methods, accompanied by the Bethe-Salpeter equation, are further developed to explore the excitation and deexcitation phenomena in detail [49,50]. Such calculations could account for the experimental measurements on excitation spectra and energy widths under a sufficiently large energy or momentum scale. However, it might be difficult to provide much information about the critical mechanisms and pictures from the numerical calculations. Whether the calculated results are suitable and reliable at low energy is worthy of detailed examinations.

ACKNOWLEDGMENTS

This material is based upon work supported by the Air Force Office of Scientific Research under Award No. FA2386-18-1-0120. We would also like to acknowledge the financial support from the Ministry of Science and Technology of the Republic of China (Taiwan) under Grant No. MOST 105-2112-M-006-002 -MY3.

---

[1] K. S. Novoselov, A. K. Geim, S. V. Morozov, D. Jiang, Y. Zhang, S. V. Dubonos, I. V. Grigorieva, and A. A. Firsov, Electric field effect in atomically thin carbon films, Science **306**, 666 (2004).

[2] K. S. Novoselov, A. K. Geim, S. V. Morozov, D. Jiang, M. I. Katsnelson, I. V. Grigorieva, S. V. Dubonos, and A. A. Firsov, Two-dimensional gas of massless Dirac fermions in graphene, Nature (London) **438**, 197 (2004).

[3] I. Pletikosić, M. Kralj, P. Pervan, R. Brako, J. Coraux, A. T. N'Diaye, C. Busse, and T. Michely, Dirac Cones and Minigaps for Graphene on Ir(111), Phys. Rev. Lett. **102**, 056808 (2009).

[4] A. H. Castro Neto, F. Guinea, N. M. R. Peres, K. S. Novoselov, and A. K. Geim, The electronic properties of graphene, Rev. Mod. Phys. **81**, 109 (2009).

[5] P. R. Wallace, The band theory of graphite, Phys. Rev. **71**, 622 (1947).

[6] Z. Jiang, E. A. Henriksen, L. C. Tung, Y. J. Wang, M. E. Schwartz, M. Y. Han, P. Kim, and H. L. Stormer, Infrared Spectroscopy of Landau Levels of Graphene, Phys. Rev. Lett. **98**, 197403 (2007).

[7] C. L. Lin, R. Arafune, R. Kawahara, M. Kanno, N. Tsukahara, E. Minamitani, Y. Kim, M. Kawai, and N. Takagi, Substrate-Induced Symmetry Breaking in Silicene, Phys. Rev. Lett. **110**, 076801 (2013).

[8] Y. H. Lai, J. H. Ho, C. P. Chang, and M. F. Lin, Magnetoelectronic properties of bilayer Bernal graphene, Phys. Rev. B **77**, 085426 (2008).

[9] C. Lin, J. Wu, Y. Ou, Y. Chiu, and M. Lin, Magneto-electronic properties of multilayer graphenes, Phys. Chem. Chem. Phys. **17**, 26008 (2015).

[10] C. Casiraghi, A. Hartschuh, E. Lidorikis, H. Qian, H. Harutyunyan, T. Gokus, K. S. Novoselov, and A. C. Ferrari, Rayleigh imaging of graphene and graphene layers, Nano Lett. **7**, 2711 (2007).

[11] Y. Kim, Y. Ma, A. Imambekov, N. G. Kalugin, A. Lombardo, A. C. Ferrari, J. Kono, and D. Smirnov, Magnetophonon resonance in graphite: High-field Raman measurements and electron-phonon coupling contributions, Phys. Rev. B **85**, 121403 (2012).

[12] M. Koshino and T. Ando, Magneto-optical properties of multilayer graphene, Phys. Rev. B **77**, 115313 (2008).

[13] C. Y. Lin, T. N. Do, Y. K. Huang and M. F. Lin, *Optical Properties of Graphene in Magnetic and Electric Fields* (IOP e-book, 2017).

[14] Y. B. Zhang, Y. W. Tan, H. L. Stormer, and P. Kim, Experimental observation of the quantum Hall effect and Berry's phase in graphene, Nature (London) **438**, 201 (2005).

[15] C. Z. Chang, J. S. Zhang, X. Feng, J. Shen, Z. C. Zhang, M. H. Guo *et al.*, Experimental observation of the quantum anomalous hall effect in a magnetic topological insulator, Science **340**, 167 (2013).

[16] C. L. Kane and E. J. Mele, Quantum Spin Hall Effect in Graphene, Phys. Rev. Lett. **95**, 226801 (2005).

[17] T. Do, C. Chang, P. Shih, and M. Lin, Stacking-enriched magneto-transport properties of few-layer graphenes, Phys. Chem. Chem. Phys. **19**, 29525 (2017).

[18] L. Li, S. Z. Lu, J. Pan, Z. Qin, Y. Wang, Y. Q. Wang, G. Cao, S. Du, and H. Gao, Buckled germanene formation on Pt(111), Adv. Mater. **26**, 4820 (2014).

[19] N. B. M. Schröter, M. D. Watson, L. B. Duffy, M. Hoesch, Y. Chen, T. Hesjedal, and T. K. Kim, Emergence of Dirac-like bands in the monolayer limit of epitaxial Ge films on Au(111), 2D Mater. **4**, 031005 (2017).

[20] M. E. Davila, L. Xian, S. Cahangirov, A. Rubio, and G. Le Lay, Germanene: A novel two-dimensional germanium allotrope akin to graphene and silicene, New J. Phys. **16**, 095002 (2014).

[21] M. Derivaz, D. Dentel, R. Stephan, M. C. Hanf, A. Mehdaoui, P. Sonnet, and C. Pirri, Continuous germanene layer on Al(111), Nano Lett. **15**, 2510 (2015).

[22] P. Vogt, P. De Padova, C. Quaresima, J. Avila, E. Frantzeskakis, M. C. Asensio, A. Resta, B. Ealet, and G. Le Lay, Silicene: Compelling Experimental Evidence for Graphenelike Two-Dimensional Silicon, Phys. Rev. Lett. **108**, 155501 (2012).

[23] L. Meng, Y. Wang, L. Zhang, S. Du, R. Wu, L. Li, Y. Zhang, G. Li, H. Zhou, W. A. Hofer, and H. J. Gao, Buckled silicene formation on Ir(111), Nano Lett. **13**, 685 (2013).

[24] A. Fleurence, R. Friedlein, T. Ozaki, H. Kawai, Y. Wang, and Y. Y. Takamura, Experimental Evidence for Epitaxial Silicene on Diboride Thin Films, Phys. Rev. Lett. **108**, 245501 (2012).

[25] F. Zhu, W. Chen, Y. Xu, C. Gao, D. Guan, C. Liu, D. Qian, S. Zhang, and J. Jia, Epitaxial growth of two-dimensional stanene, Nat. Mater. **14**, 1020 (2015).

[26] Z. Ni, Q. Liu, K. Tang, J. Zheng, J. Zhou, R. Qin, Z. Gao, D. Yu, and J. Lu, Tunable bandgap in silicene and germanene, Nano Lett. **12**, 113 (2012).

[27] C. C. Liu, H. Jiang, and Y. Yao, Low-energy effective Hamiltonian involving spin-orbit coupling in silicene and two-dimensional germanium and tin, Phys. Rev. B **84**, 195430 (2011).

[28] M. Ezawa, A topological insulator and helical zero mode in silicene under an inhomogeneous electric field, New J. Phys. **14**, 033003 (2012).

[29] S. M. Huang, S. T. Lee, and C. Y. Mou, Ferromagnetism and quantum anomalous Hall effect in one-side-saturated buckled honeycomb lattices, Phys. Rev. B **89**, 195444 (2014).

[30] J. Zheng, F. Chi, and Y. Guo, Exchange and electric fields enhanced spin thermoelectric performance of germanene nanoribbon, J. Phys.: Condens. Matter **27**, 295302 (2015).

[31] V. Ongun Öçelik, E. Durgun, and S. Ciraci, New phases of germanene, J. Phys. Chem. Lett. **5**, 2694 (2014).

[32] C. Heske, R. Treusch, F. J. Himpsel, S. Kakar, L. J. Terminello, H. J. Weyer, and E. L. Shirley, Band widening in graphite, Phys. Rev. B **59**, 4680 (1999).

[33] A. Bostwick, T. Ohta, T. Seyller, K. Horn, and E. Rotenberg, Quasiparticle dynamics in graphene, Nat. Phys. **3**, 36 (2007).

[34] E. H. Hwang and S. Das Sarma, Dielectric function, screening, and plasmons in two-dimensional graphene, Phys. Rev. B **75**, 205418 (2007).

[35] J. H. Ho, C. L. Lu, C. C. Hwang, C. P. Chang, and M. F. Lin, Coulomb excitations in AA- and AB-stacked bilayer graphites, Phys. Rev. B **74**, 085406 (2006).

[36] C. J. Tabert and E. J. Nicol, Dynamical polarization function, plasmons, and screening in silicene and other buckled honeycomb lattices, Phys. Rev. B **89**, 195410 (2014).

[37] H. R. Chang, J. Zhou, H. Zhang, and Y. Yao, Probing the topological phase transition via density oscillations in silicene and germanene, Phys. Rev. B **89**, 201411 (2014).

[38] P. H. Shih, Y. H. Chiu, J. Y. Wu, F. L. Shyu, and M. F. Lin, Coulomb excitations of monolayer germanene, Sci. Rep. **7**, 40600 (2017).

[39] G. D. Mahan, *Many-Particle Physics*, 3rd ed. (Plenum, New York, 2000).

[40] A. V. Chaplik, Energy Spectrum and Electron Scattering Processes in Inversion Layers, J. Exp. Theor. Phys. **33**, 977 (1971).

[41] G. F. Giuliani and J. J. Quinn, Lifetime of a quasiparticle in a two-dimensional electron gas, Phys. Rev. B **26**, 4421 (1982).

[42] T. Ando, Screening effect and impurity scattering in monolayer graphene, J. Phys. Soc. Jpn. **75**, 074716 (2006).

[43] O. Roslyak, G. Gumbs, and D. Huang, Plasma excitations of dressed Dirac electrons in graphene layers, J. Appl. Phys. **109**, 113721 (2011).

[44] Q. Li and S. Das Sarma, Finite temperature inelastic mean free path and quasiparticle lifetime in graphene, Phys. Rev. B **87**, 085406 (2013).

[45] E. H. Hwang, B. Y. K. Hu, and S. Das Sarma, Inelastic carrier lifetime in graphene, Phys. Rev. B **76**, 115434 (2007).

[46] L. Algharagholy, S. W. D. Bailey, T. Pope, and C. J. Lambert, Germanene and stanene on two-dimensional substrates: Dirac cone and Z_2 invariant, Phys. Rev. B **86**, 075427 (2012).

[47] Z. Ni, E. Minamitani, Y. Ando, and S. Watanabe, The electronic structure of quasi-free-standing germanene on monolayer MX (M = Ga, In; X = S, Se, Te), Phys. Chem. Chem. Phys. **17**, 19039 (2015).

[48] C. W. Chiu, S. H. Lee, S. C. Chen, and M. F. Lin, Electronic excitations in doped monolayer graphenes, J. Appl. Phys. **106**, 113711 (2009).

[49] C.-H. Park, F. Giustino, C. D. Spataru, M. L. Cohen, and S. G. Louie, Erratum: First-Principles Study of Electron Linewidths in Graphene, Phys. Rev. Lett. **102**, 189904(E) (2009).

[50] L. Hung, F. H. da Jornada, J. Souto-Casares, J. R. Chelikowsky, S. G. Louie, and S. Ogut, Excitation spectra of aromatic molecules within a real-space GW-BSE formalism: Role of self-consistency and vertex corrections, Phys. Rev. B **94**, 085125 (2016).